











RESEARCH ARTICLE | DECEMBER 16 2021

## Synchronized beamline at FLASH2 based on high-order harmonic generation for two-color dynamics studies

E. Appi ; C. C. Papadopoulou ; J. L. Mapa; C. Jusko; P. Mosel; A. Schoenberg; J. Stock; T. Feigl; S. Ališauskas ; T. Lang; C. M. Heyl; B. Manschwetus ; M. Brachmanski; M. Braune ; H. Lindenblatt ; F. Trost; S. Meister ; P. Schoch ; A. Trabattoni; F. Calegari; R. Treusch ; R. Moshhammer; I. Hartl ; U. Morgner; M. Kovacev



Rev. Sci. Instrum. 92, 123004 (2021)  
<https://doi.org/10.1063/5.0063225>



CrossMark



www.ssi-instrument.com

- PXIe module Lock-in Amplifier
- Multi-channel Lock-in Amplifier
- Up to 8 demodulators
- Toolset: Scope, FFT, PID, Sweeper

### Customize your own Lock-in Amplifier

DC to 300MHz frequency



# Synchronized beamline at FLASH2 based on high-order harmonic generation for two-color dynamics studies

Cite as: Rev. Sci. Instrum. 92, 123004 (2021); doi: 10.1063/5.0063225  
Submitted: 13 July 2021 • Accepted: 26 November 2021 •  
Published Online: 16 December 2021



View Online



Export Citation



CrossMark

E. Appi,<sup>1,2,3,a)</sup> C. C. Papadopoulou,<sup>4</sup> J. L. Mapa,<sup>1,2,3</sup> C. Jusko,<sup>1,2,3</sup> P. Mosel,<sup>1,2,3</sup> A. Schoenberg,<sup>4</sup> J. Stock,<sup>5</sup> T. Feigl,<sup>6</sup> S. Ališauskas,<sup>4</sup> T. Lang,<sup>4</sup> C. M. Heyl,<sup>4,7,8</sup> B. Manschwetus,<sup>4</sup> M. Brachmanski,<sup>4</sup> M. Braune,<sup>4</sup> H. Lindenblatt,<sup>9</sup> F. Trost,<sup>9</sup> S. Meister,<sup>9</sup> P. Schoch,<sup>10</sup> A. Trabattoni,<sup>11</sup> F. Calegari,<sup>11,12</sup> R. Treusch,<sup>4</sup> R. Moshhammer,<sup>9</sup> I. Hartl,<sup>4</sup> U. Morgner,<sup>1,2,3</sup> and M. Kovacev<sup>1,2,3</sup>

## AFFILIATIONS

<sup>1</sup>Institut für Quantenoptik, Leibniz Universität Hannover, Hannover 30167, Germany

<sup>2</sup>Cluster of Excellence PhoenixD, Hannover 30167, Germany

<sup>3</sup>EXC 2123/1 QuantumFrontiers, Hannover 30167, Germany

<sup>4</sup>DESY, Hamburg 22607, Germany

<sup>5</sup>Carl Zeiss AG, Oberkochen 73446, Germany

<sup>6</sup>optiX fab GmbH, Jena 07745, Germany

<sup>7</sup>Helmholtz-Institut Jena, Jena 07743, Germany

<sup>8</sup>GSI Helmholtzzentrum für Schwerionenforschung GmbH, Darmstadt 64291, Germany

<sup>9</sup>Max-Planck-Institut für Kernphysik, Heidelberg 69117, Germany

<sup>10</sup>Institut für Umweltphysik, Ruprecht-Karls-Universität Heidelberg, Heidelberg 69120, Germany

<sup>11</sup>Center for Free-Electron Laser Science CFEL, DESY, Hamburg 22607, Germany

<sup>12</sup>Physics Department, University of Hamburg, Hamburg 22761, Germany

<sup>a)</sup> Author to whom correspondence should be addressed: [appi@iqo.uni-hannover.de](mailto:appi@iqo.uni-hannover.de)

## ABSTRACT

We present the design, integration, and operation of the novel vacuum ultraviolet (VUV) beamline installed at the free-electron laser (FEL) FLASH. The VUV source is based on high-order harmonic generation (HHG) in gas and is driven by an optical laser system synchronized with the timing structure of the FEL. Ultrashort pulses in the spectral range from 10 to 40 eV are coupled with the FEL in the beamline FL26, which features a reaction microscope (REMI) permanent endstation for time-resolved studies of ultrafast dynamics in atomic and molecular targets. The connection of the high-pressure gas HHG source to the ultra-high vacuum FEL beamline requires a compact and reliable system, able to encounter the challenging vacuum requirements and coupling conditions. First commissioning results show the successful operation of the beamline, reaching a VUV focused beam size of about 20  $\mu\text{m}$  at the REMI endstation. Proof-of-principle photo-electron momentum measurements in argon indicate the source capabilities for future two-color pump-probe experiments.

© 2021 Author(s). All article content, except where otherwise noted, is licensed under a Creative Commons Attribution (CC BY) license (<http://creativecommons.org/licenses/by/4.0/>). <https://doi.org/10.1063/5.0063225>

## I. INTRODUCTION

The advent of free-electron lasers (FELs) provided a powerful tool for the investigation of a large variety of light-matter interactions with unprecedented capabilities.<sup>1,2</sup> In this context,

unique parameters such as high photon flux (typically  $10^{14}$  photons/pulse), spectral tunability from infrared to hard x-rays, and femtosecond pulse duration allowed for outstanding achievements in the field of ultrafast time-resolved spectroscopy.<sup>3-5</sup> For example, extreme-ultraviolet (XUV) FELs are key elements for the

investigation of valence photoionization dynamics occurring in molecules,<sup>6,7</sup> while x-ray FELs have given access to core electron excitation and probing in atoms and molecules<sup>8,9</sup> and to the investigation of dynamical structures through time-resolved diffraction techniques.<sup>10–13</sup> Recently, FEL pulses with sub-femtosecond duration were obtained,<sup>14</sup> paving the way for a new generation of attosecond experiments.<sup>15</sup>

In the last 20 years, ultrashort laser pulses have been routinely produced through high-order harmonic generation (HHG),<sup>16–20</sup> leading to important breakthroughs in the investigation of ultrafast electron dynamics in matter.<sup>21–24</sup> In a typical HHG setup, an ultra-intense laser is focused ( $I > 10^{14}$  W/cm<sup>2</sup>) onto a gas-phase atomic target, triggering a strong-field photo-interaction: a valence electron is first ejected from the atom through tunneling, then accelerated by the external field, and eventually driven back to the parent ion.<sup>25,26</sup> The radiative electron recombination results in the emission of light bursts, with durations down to a few tens of attoseconds. In contrast to FELs, HHG-based sources usually present a lower photon flux (generation efficiency  $\approx 10^{-6}$ ), while providing high coherence and ultra-broadband spectra from the vacuum ultraviolet (VUV) to the soft x-ray region, as well as compact setups and the natural flexibility of table-top sources.<sup>27–29</sup>

Given the complementary potential of FELs and HHG-based sources, the possibility of combining the two in a novel pump-probe setup is of high interest as a tool to expand the parameter space of femtosecond time-resolved spectroscopy. However, such an apparatus also presents several challenges: a compact and reliable HHG setup needs to be integrated into the ultra-high vacuum FEL beamline. Furthermore, a concept for synchronizing and combining the two beams on the target has to be developed, handling the different spectral properties and the low fluence of the HHG radiation in contrast to the FEL. In addition, while FEL beamlines typically have long propagation arms, it is desirable to produce the HHG radiation as close as possible to the experimental endstation. That way, the HHG photon flux is not further reduced through long propagation and multiple steering optics, maximizing the available HHG intensity at the interaction point. Furthermore, short propagation arms improve the passive interferometric stability of the pump-probe setup.

In this work, we describe the implementation of a VUV source based on HHG at the free-electron laser FLASH2 (DESY).<sup>30,31</sup> In particular, we focus on the technical aspects, design, and simulations, which allowed the above-mentioned challenges to be addressed. The setup described here represents the first permanent FEL-HHG pump-probe apparatus for time-resolved experiments. Given the importance of such a benchmark, this presentation provides specific strategies for the development of future combined FEL-HHG setups.

This article is organized as follows: Sec. II shows the beamline design, where all the technical details considered during the design phase are presented for each part of the setup separately; Sec. III describes the experimental conditions, focusing on the implementation of the design; and Sec. IV presents and discusses briefly the preliminary results in the reaction microscope (REMI). Finally, the potential for future experiments employing this setup is described in Sec. V. A detailed presentation and discussion about the performance of the VUV source can be found in our previous publication.<sup>32</sup>

## II. BEAMLINE DESIGN

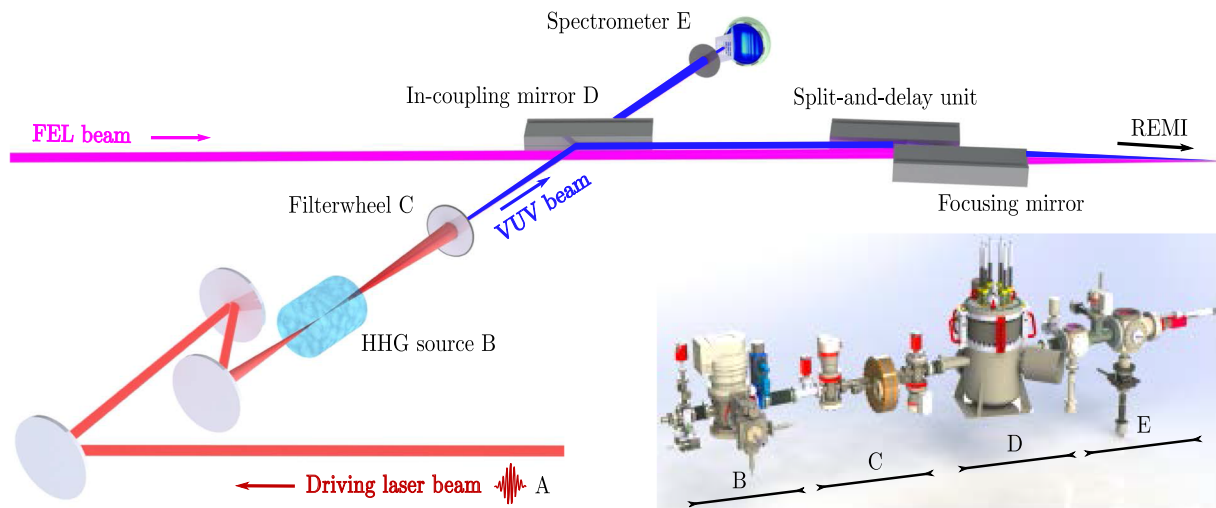
The VUV setup installed at the free-electron laser FLASH2 is integrated into the beamline FL26, which features a permanent reaction microscope<sup>33</sup> (REMI) endstation. Several pump-probe experiments employing the FEL beam only or in combination with near-infrared (NIR) optical pulses have been so far carried out in the reaction microscope, targeting ultrafast dynamics in atomic and molecular systems. A complete description of the endstation and its capabilities can be found in the works of Schmid *et al.*<sup>34</sup> and Meister *et al.*<sup>35</sup>

Figure 1 depicts a schematic of the novel VUV experimental apparatus. The VUV source (position B in Fig. 1) is based on high-order harmonic generation in gas, and it is driven by the optical pump-probe laser (position A) of the FLASH2 experimental hall.<sup>36</sup> The generated radiation propagates in the vacuum beamline toward a double filterwheel (position C), where filters of different materials and thicknesses can be inserted in the beam path to block the remaining driving light or to select the specific spectral region of interest. The VUV radiation is then coupled with the FEL beam by means of a hyperboloidal in-coupling mirror (position D) and consequently focused into REMI for two-color VUV-XUV pump-probe studies. The temporal delay between VUV and FEL pulses can be controlled either by a split-and-delay unit (SDU) or by the laser synchronization system. Additionally, the in-coupling mirror can be completely moved out of the beam path in order to allow for the VUV radiation to reach an in-line spectrometer (position E) for characterization of the spectral components and pulse energy measurements.

### A. Driving laser optical setup

The optical pump-probe laser of the FLASH2 hall is an optical parametric chirped pulse amplification (OPCPA) system, optically synchronized with the timing pattern of the FEL.<sup>37</sup> The free-electron laser FLASH2 operates in burst mode, emitting macro-pulses at 10 Hz containing up to 800 micro-pulses with a tunable repetition rate. A 100 kHz intra-burst repetition rate is typically used at the REMI endstation. The laser system is controlled by the same master timing system of the FLASH facility and is thus fully synchronized with the FEL at its generation point. It delivers near-infrared pulses (central wavelength tunable from 680 to 920 nm) to the experimental endstation via a 40 m long relay-imaging transport vacuum beamline. The high intra-burst repetition rate of the laser system limits the available pulse energy, which is further reduced by beam transport losses induced by broadband optics, to a few hundred  $\mu$ J at the endstation. Therefore, the optical setup installed close to the HHG source has to be optimized to achieve the required intensity for high-order harmonic generation.

An active drift stabilization system is used after the transport line to control the beam pointing of the laser beam. The stabilization system is based on the feedback provided by a camera setup to actively correct the alignment of two piezo-actuated mirrors (M1 and M2 in Fig. 2) and, as a consequence, the alignment of the beam. The laser pulses are then compressed by using a pair of double-chirped mirrors (DCMs). The beam enters the compressor, and after eight bounces on the DCMs, it is back-reflected and lowered in height. After eight additional bounces and a total negative dispersion of  $-1200$  fs<sup>2</sup>, the beam leaves the compressor and propagates



**FIG. 1.** Schematic concept of the presented beamline. The VUV generation is driven by an optical infrared laser (A) focused in the gas-filled cell (HHG source, B). A double filterwheel (C) allows us to block the remaining driving light. The VUV radiation is then coupled with the FEL beam by using an in-coupling mirror (D) or spectrally resolved by using an in-line spectrometer (E). The inset shows a 3D CAD drawing of the vacuum VUV beamline.

toward the next section of the optical setup after being reflected by a D-shaped mirror. With this configuration, a pulse duration of about 15 fs (FWHM) is measured.

In order to optimize the focusing conditions for the generation of VUV radiation, a telescope for astigmatism correction has been installed (mirrors F1 and F2 in Fig. 2, placed at a distance of 85 mm, with focal lengths of 250 mm and  $-375$  mm, respectively). Via a camera monitoring a reflected part of the beam at the virtual focus position outside the HHG chamber, the angle of incidence on the mirrors is optimized to minimize the astigmatism of the focused beam in the HHG source.

A periscope guides the beam close to the HHG source, where pulses with energy of up to  $225 \mu\text{J}$  are focused in the gas medium by using a second telescope (mirrors F3 and F4). The focusing optics

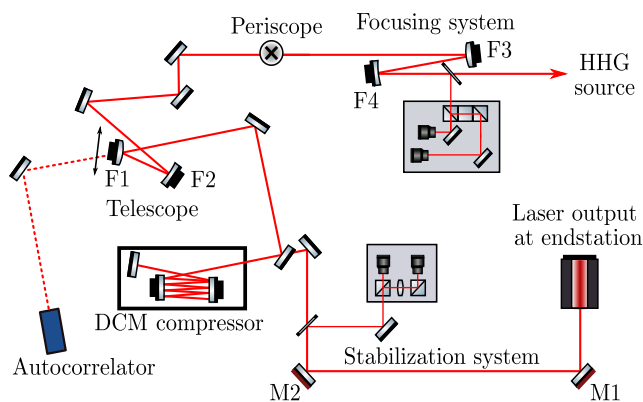


**FIG. 2.** Schematic of the driving laser optical setup for HHG. After transport, the laser pulses are compressed and focused into the HHG source. A stabilization system based on beam cameras and piezo-actuated mirrors is used to minimize the beam pointing. A second camera system is used as reference for alignment.

can be chosen according to the laser performance in order to reach an intensity in the range of  $10^{14} \text{ W/cm}^2$  required for the harmonic generation process. A commonly used focusing system consists of a 150 mm defocusing mirror and a  $-200$  mm focusing mirror at a distance of 165 mm (effective focal length:  $\sim 410$  mm).

A camera system placed close to the source is used as reference for the alignment of the driving laser beam through the VUV beamline and for monitoring the virtual focus as mentioned before.

## B. HHG source

The ultrashort pulses of the optical laser are focused into a gas medium contained in a semi-infinite gas cell (SIGC) inserted into a vacuum chamber, indicated as “HHG chamber”. This configuration allows for an abrupt pressure transition between the gas medium and the vacuum side, simplifying the differential pumping system needed in order to meet the beamline vacuum requirements (see Sec. III A). Other configurations for the generation of high-order harmonics, such as short gas cell or gas nozzle, can be implemented, but the design has to be adjusted to ensure the correct operational pressure range for long-term measurements.

In the present source, the entrance of the SIGC consists of a 1 mm thick fused silica laser window connected to the vacuum system [see Fig. 3(a)]. The pressure of the noble gas inserted in the cell can vary in a range from tens to hundreds of mbar, depending on the generation conditions, and is actively controlled via a proportional integral derivative proportional-integral-derivative (PID) feedback by a regulating valve (EVR 116, Pfeiffer) connected to a roughing vacuum pump. During operation, the pressure oscillations in the gas cell are kept below 0.2 mbar (typical pressure in SIGC:  $\sim 100$  mbar). The gas cell reaches the beam focus in the center of the HHG chamber by a 19 cm long tube (red tube in Fig. 3). The cell's total length of 30 cm ensures that nonlinear effects on the input laser window are avoided. The cell terminates with a 0.5 mm thick



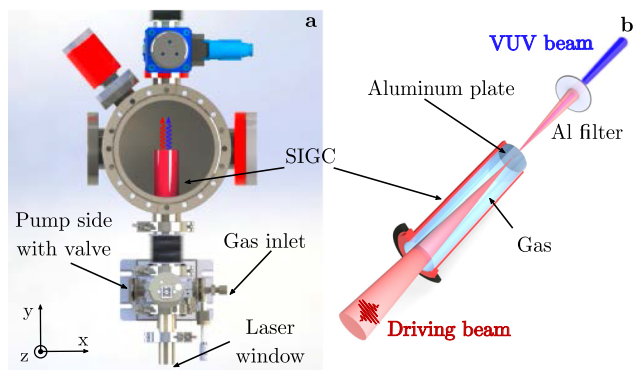


**FIG. 3.** (a) Top view of the HHG source design. A semi-infinite gas cell (SIGC) can be moved along the  $y$  axis to optimize the VUV generation conditions. (b) Working principle of HHG in a SIGC. The focused driving beam drills a  $<100\ \mu\text{m}$  hole in an Al termination plate, enabling the VUV beam propagation.

aluminum plate, in which the focused laser beam drills a  $<100\ \mu\text{m}$  hole, enabling the propagation of the generated VUV radiation along the beamline. This small hole also acts as a first differential pumping stage, separating the high-pressure gas cell from the rest of the vacuum beamline. It is one of the several differential pumping stages implemented in the setup in order to reach the required operational pressure at the REMI endstation in the  $10^{-11}$  mbar range. A linear translation stage (LT1, Thorlabs) allows us to move the gas cell along the beam propagation direction ( $y$  axis) by  $\pm 2.5$  cm, and it is used for optimization of the distance between the aluminum plate and the laser focus position.

### C. Filterwheel

After the generation process, the VUV beam co-propagates in the vacuum beamline together with the remaining fundamental near-infrared light, which, for most applications, needs to be blocked. To this end, we use a rotatable double filterwheel, where filters of different thicknesses and materials can be installed. The design includes two wheels that can be rotated independently of each other. Each wheel consists of a stainless steel disk with multiple openings connected to a manual rotatable feedthrough, where seven filters of 10 mm diameter and four filters of 15 mm diameter can be installed for a total of 11 filters per wheel. One opening is left free in both wheels to allow for the propagation of unfiltered radiation. Thanks to the double-wheel design, filters can be combined together to select a specific spectral window of interest from the full harmonic spectrum, giving the possibility to tune the spectrum delivered to the experiment.

In order to suppress the fundamental near-infrared light, a  $0.1\ \mu\text{m}$  thick aluminum filter with a supporting nickel mesh is used. Due to the sharp edge around 70 nm in its transmission curve,<sup>38</sup> the Al filter cuts out the NIR beam while allowing for the propagation of maximum 79% of the harmonic power for orders  $>11$  in the spectral range 20–60 nm. In combination with the Ni mesh (5  $\mu\text{m}$  thickness, 86% transmission, and 36  $\mu\text{m}$  pitch, Lebow Company), the calculated transmission, omitting any oxidation due to exposure to air, is  $\sim 68\%$  in the above-mentioned range. Free-standing  $0.1\ \mu\text{m}$  Al filters are also available and are planned to be installed in the future in order to increase the VUV transmission.

### D. In-coupling chamber

A vacuum chamber (Fig. 4) designed and manufactured by FMB-Berlin GmbH, which contains the “in-coupling mirror”, is installed at the intersection point of the VUV and the FEL beams (position D in Fig. 1). The chamber connects the two beamlines at  $16^\circ$  angle such that the grazing angle of the VUV beam on the mirror is fixed at  $8^\circ$ , ensuring a high reflectivity on the carbon-coated mirror ( $\sim 80\%$ ). The VUV beam propagates 7.5 mm higher than the FEL so that the latter passes under the mirror, being partially blocked (see Sec. II F).

Following a similar design of the other XUV optics present at the endstation, the in-coupling mirror is mounted on a holder connected to a hexapod kinematics structure, which grants full control on the mirror positioning. The hexapod structure is connected, via the top flange, to six linear actuators outside of the vacuum chamber. A detailed description of the kinematics can be found in the work of Noll *et al.*<sup>39</sup> and Schmid *et al.*<sup>34</sup>

In order to access the in-line spectrometer, the in-coupling mirror has to be moved completely out of the beam path. This way, the generated VUV beam can be characterized without the need of any additional reflecting optics. To this end, three options were considered: a vertical lift of the mirror by moving the hexapod mechanism, a vertical lift of the whole top flange without movement of the hexapod, or a tilt of the top flange. The latter two options would require a bellows to connect the top flange with the main part of the chamber. In general, the hexapod mechanisms are designed for accurate

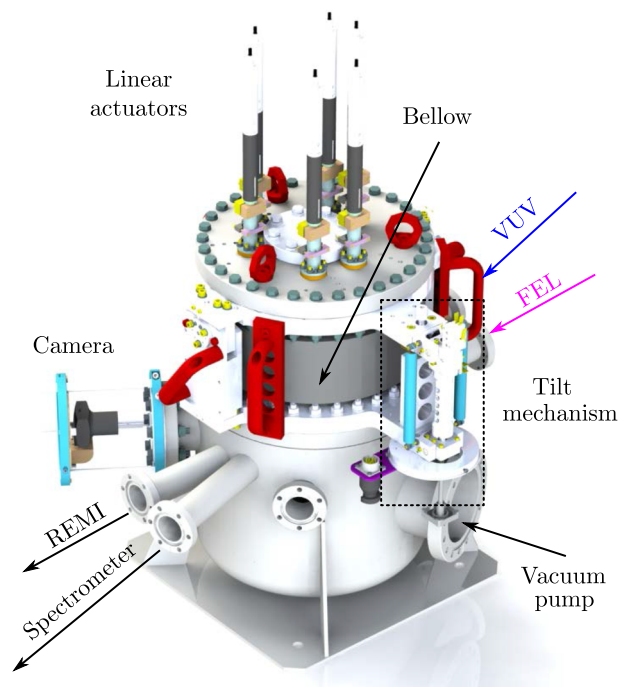


**FIG. 4.** In-coupling chamber design. The chamber connects the VUV setup to the FEL beamline, giving access to the experimental endstation and to the in-line spectrometer. Linear actuators on the top flange control the hexapod kinematics structure, on which the mirror is mounted. A tilt mechanism and a bellows allow for the movement of the mirror out of the beam paths.

rotational and translational alignment movements but not for long travel. In this particular case, the vertical movement of the hexapod is limited to 5 mm by the springs connecting it with the actuators, but the required travel distance in order to completely unblock the VUV beam, also taking into account the mirror mount, is  $\sim 28$  mm. A much more advanced and costly combination of hexapod and linear actuators would be indispensable to achieve such a long travel range. On the other hand, a vertical movement of the top flange would correspond to a load of more than 500 kg because of the atmospheric pressure plus the weight of the actual components and the bellow forces. The option of tilting the flange without changing the relative position of the mirror (see Fig. 5) makes use of the cancellation of the vacuum forces to reduce the load. In practice, by means of a linear actuator with a maximum load of  $\sim 50$  kg (LGA421S14-B-TJBA-038, Nanotec) placed on the side of the bellow, a tilt of  $6^\circ$  (maximum  $8^\circ$  before collisions occur) can be achieved, which allows for the entire VUV beam to propagate up to the in-line spectrometer.

### E. In-line spectrometer

In order to detect the VUV signal and to resolve the harmonic spectrum, an in-line spectrometer is installed behind the in-coupling mirror (see position E in Fig. 1). Due to the limited space available in the experimental hall and to the small angle between the VUV and FEL beamlines, it was necessary to implement a compact geometry. The use of a transmission diffraction grating allows for an overall length of the assembly of only 1.26 m.

The assembly (Fig. 6) consists of two vacuum cubes with multiple feedthroughs for a complete free-standing setup, where each component can be moved with respect to the others. In the first vacuum cube, an XUV photodiode (AXUV576, OptoDiode) is placed, which is used to measure the harmonic pulse energy. The large active area of  $24 \times 24$  mm<sup>2</sup> ensures the detection of the whole divergent VUV beam. The photodiode is mounted on a custom-made holder [shown in inset (a) of Fig. 6], which also includes a Ni-mesh supported Al filter placed in front of the detector, necessary to block any remaining near-infrared scattered light. The holder is connected to a vertical linear feedthrough in order to be moved in or out of

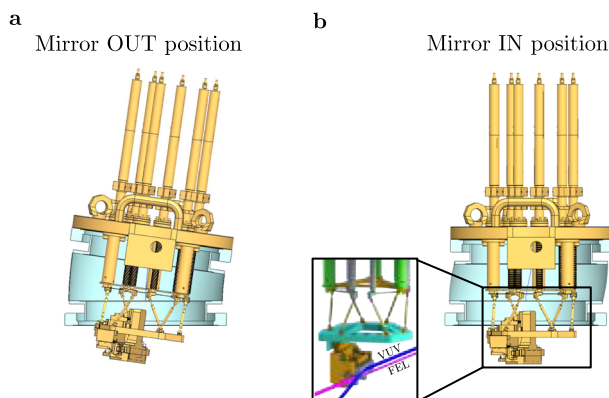


**FIG. 5.** Schematic of the inner structure of the in-coupling chamber. A tilt of the top flange allows for a movement of the mirror (a) out of the VUV beam path in order to reach the in-line spectrometer or (b) in the VUV beam path to couple it with the FEL.

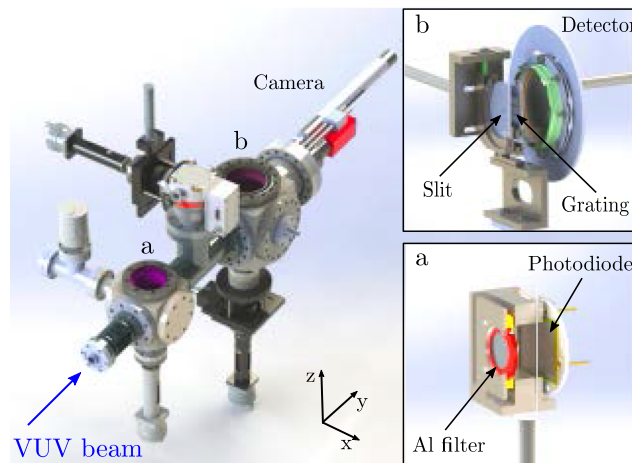


**FIG. 6.** Design of the in-line spectrometer, which includes a XUV photodiode [inset (a)] and a transmission grating assembly [inset (b)].

the beam path. In the latter case, the VUV beam reaches the second vacuum cube.

In this second part, a transmission grating spatially separates the spectral components of the VUV beam, which are detected by using a double microchannel plate (MCP) assembly combined with a phosphor screen (DD 2561 ZV, Proxivision). The harmonic spectrum is recorded by using a camera (acA2040-25gm, Basler), placed outside the vacuum chamber, for subsequent data analysis. The grating's period has to be chosen according to the expected harmonic spectral range, the dimensions of the MCP assembly, and the grating-detector distance. Instead of a single transmission grating, we have installed a free-standing chip, where gratings of different periods are available. A description of the grating chip fabrication and performance can be found in the work of Goh *et al.*<sup>40</sup> The grating of interest can be easily selected by placing a slit directly in front of it [inset (b) of Fig. 6]. All the components (slit, grating chip, and detector) are mounted on separate linear feedthroughs for optimization of their relative positions. The slit and the grating chip can be moved in the  $x$ - $z$  plane, thanks to a second translation stage connected to the linear feedthroughs. The detector, on the other hand, can be moved along the  $y$  axis (1–15 cm from the grating chip) to allow for flexibility in the grating-detector distance. Taking advantage of the zero-degree incidence angle of this geometry and considering the 25 mm diameter of the detector used, both the zero and first order of diffraction are detected, ensuring an alignment-independent wavelength calibration, which only depends on the grating period and the grating-detector distance.

In general, the wavelength calibration is performed by taking into account the grating equation, which can be expressed as

$$m\lambda_x = d \sin\left(\arctan \frac{X - x_0}{L}\right), \quad (1)$$

where  $m$  is the diffraction order,  $\lambda_x$  is the wavelength calibrated axis of the spectrum,  $d$  is the grating period,  $X$  is the camera axis along the resolved spectrum,  $x_0$  is the position of the zero order of diffraction, and  $L$  is the distance between the grating and the detector. The

parameters  $x_0$  and  $L$  can be measured directly, or they can be estimated from the recorded spectrum by assuming the wavelengths of two consecutive peaks and measuring the distance between them. The uncertainties of these two parameters play a major role in the final calibration error, which can be estimated by error propagation. We estimate the relative wavelength calibration error at about 6%. The calibration is then tested with the insertion of an aluminum filter in the beam path, which, as already mentioned, blocks harmonic orders below 11th.

### F. Imaging of the VUV beam in REMI

The main objective of the beamline design is to maximize the VUV radiation delivered into the REMI endstation for pump-probe experiments. Therefore, the specifications of the in-coupling mirror had to be carefully selected based on the expected parameters of the VUV beam, such as source size, divergence, and spectral range. Since the new VUV source is integrated in a previously existing FEL endstation, the focusing conditions into REMI are fixed by the flat split-and-delay mirror and the ellipsoidal mirror already present at FL26. The goal of the in-coupling mirror is to allow for the propagation of both the VUV and the FEL beam, while ensuring their spatial overlap in REMI. To this end, an off-axis hyperboloidal mirror (OptiXfab GmbH) is used. It has a rectangular face of  $100 \times 15 \text{ mm}^2$  and is placed in the in-coupling chamber at 1500 mm distance from the VUV source point. A 30 nm ( $\pm 5\%$ ) carbon coating layer ensures an almost constant reflectivity close to 80% at a grazing angle of  $8^\circ$  for photon energies from 10 to 40 eV,<sup>38</sup> i.e., wavelengths from 30 to 120 nm.

The geometrical beam paths of the VUV and FEL beams in the optical setup are sketched in Fig. 7. The FEL beam propagates from source point S1 to the split-and-delay unit (SDU) and is reflected on ellipsoidal mirror M2. The S1–M2 distance is around 85 m. Due to the reflection from the split-and-delay unit, the FEL beam seems to come from virtual source point S', before being focused by M2. The

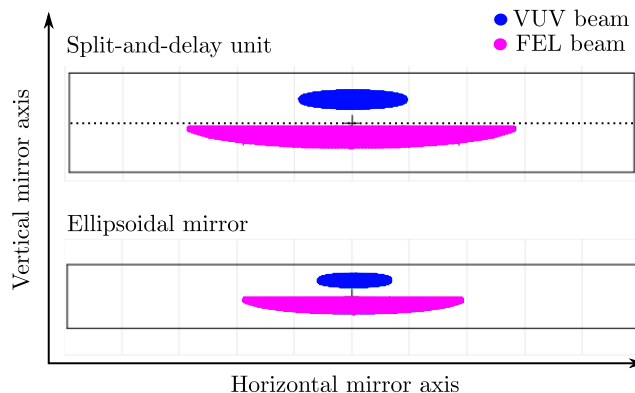


**FIG. 8.** Ray tracing simulation of the beams' footprints on the split-and-delay unit (top) and ellipsoidal mirror (bottom). A truncation of the FEL beam due to the insertion of the in-coupling mirror is accounted for. The clear aperture dimensions are  $120 \times 10.5 \text{ mm}^2$  and  $180 \times 20 \text{ mm}^2$  for each part of the split-and-delay unit and the ellipsoidal mirror, respectively.<sup>34</sup>

ellipsoidal mirror allows for a stigmatic imaging of the FEL source point into the REMI interaction region (position F, Fig. 7). The VUV beam starts propagating from source point S2. To ensure the superposition of the two beams in REMI, the hyperboloidal mirror is designed to create a virtual VUV source point, which coincides with S1. Therefore, the VUV beam is reflected by the split-and-delay unit and the ellipsoidal mirror in the same way as the FEL beam. From a mathematical point of view, the selected conical mirrors have a perfect imaging performance for an ideal point source under the assumption of geometrical optics. The real focal dimensions in REMI are broadened by the imperfections of the real manufactured mirrors, residual positioning errors, and the

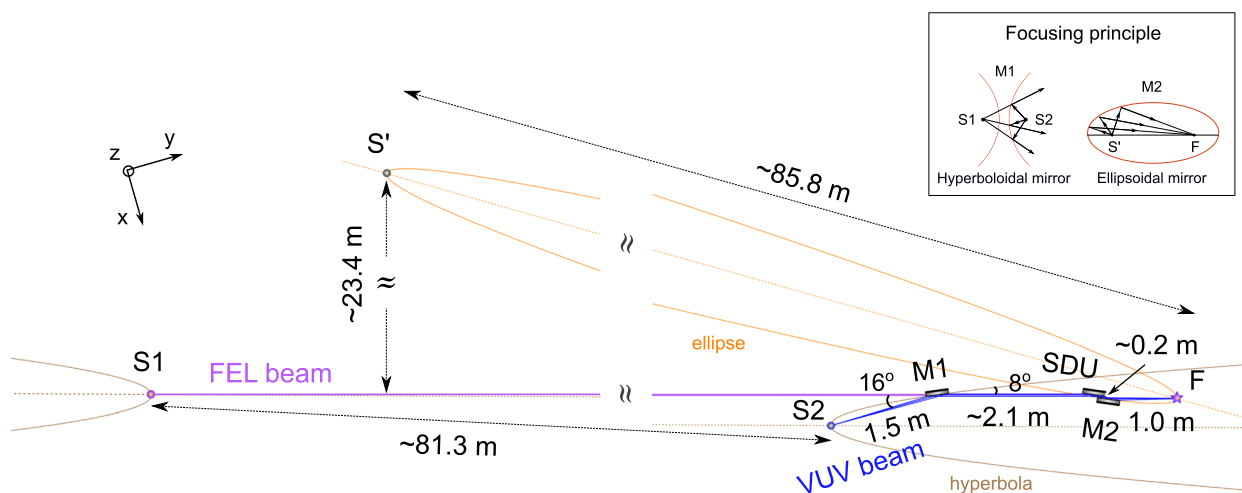


**FIG. 7.** Overview of the focusing and imaging principle of the FEL and VUV beams. The dimensions and angles are in scale. The FEL and VUV source points are located at S1 and S2, respectively. The hyperboloidal mirror M1 creates a virtual source point of the VUV beam at S1 (see “focusing principle” in the inset), which is subsequently shifted to S' by using the split-and-delay unit. The two beams are focused by ellipsoidal mirror M2 on F, which coincides with the REMI center. It should be noted that the distances between the vertices and the foci of the hyperbola and the ellipse are below the resolution of this figure ( $\sim 2 \text{ cm}$ ).

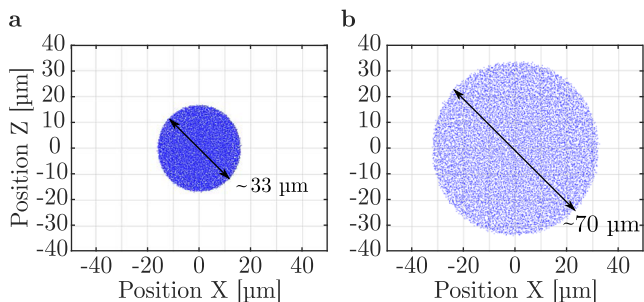


**FIG. 9.** Ray tracing simulations of the VUV focus size in REMI for (a) 50  $\mu\text{m}$  and (b) 100  $\mu\text{m}$  source diameter, respectively. A half-angle divergence of 1 mrad is considered.

convolution, according to the system’s magnification, with the finite size of the corresponding source areas.

Knowing the distance between the VUV source point and the in-coupling mirror and the specifications of the optics already present in the FEL beamline (flat split-and-delay mirror and ellipsoidal focusing mirror), ray tracing simulations of the beams in the beamline were performed. Figure 8 depicts the simulated footprints of the VUV and FEL beams on the beamline mirrors. The FEL beam is simulated partially truncated due to the presence of the hyperboloidal mirror, which blocks the top part of the beam. This effect can be minimized by aligning the FEL beam lower than its nominal position in the center of the beamline or by placing an aperture to block part of the FEL beam before the in-coupling chamber.

Since the positioning of the split-and-delay unit and the ellipsoidal mirror is already determined by the FEL beam, the alignment of the hyperboloidal in-coupling mirror is critical for the correct focusing of the VUV beam into REMI. The most sensitive adjustment is the orientation of the hyperboloidal around the vertical z axis. A tilt of  $0.1^\circ$ , i.e., a change in the grazing incidence angle,

leads to a shift of the image in the focus point of 3.7 mm. Fortunately, this can be partly compensated by a re-adjustment of the VUV beam alignment. The final VUV focus size in REMI depends on the initial source size and on the magnification of the optical system. Considering a VUV divergence of 1 mrad, the simulated focus diameter in REMI is about 33  $\mu\text{m}$  and 70  $\mu\text{m}$  for a 50 and a 100  $\mu\text{m}$  source diameter, respectively (see Fig. 9).

### G. Laser and vacuum interlock concepts

The integration of a laser-driven VUV source into a FEL end-station, hosting a reaction microscope, has to meet several requirements related both to the safety of users and to the protection and preservation of the operative conditions of all the setup parts, including the FLASH machine and REMI. For this reason, two interlock systems were developed and implemented.

The laser interlock ensures that the surrounding area is protected from hazardous optical laser radiation. The optical setup and part of the VUV beamline are enclosed in a laser-safe hutch, where only authorized trained personnel has access. The HHG source can be operated only if all the safety requirements are fulfilled. Two laser-safety shutters (NIR-VUV non-transparent shutters with steel plates) block the beam at the end of the beam transport line inside the laser hutch and before the in-coupling chamber at the crossing point of the hutch with the VUV beamline. They are operated by two key-activated panels located inside the hutch to prevent accidental opening from outside. The two shutters can be independently operated. When the beam is delivered into the hutch (first shutter open), the “Laser ON” sign outside the door lights up. At the same time, the door is kept closed by magnets, which can be deactivated for a limited time only by using a DESY Access Handling System (DACHS) card to enter the hutch without closing the shutters. Emergency buttons on both sides of the door will close the first shutter and release the door. When the interlock is triggered by some condition violation (door remained open for a long time, emergency buttons

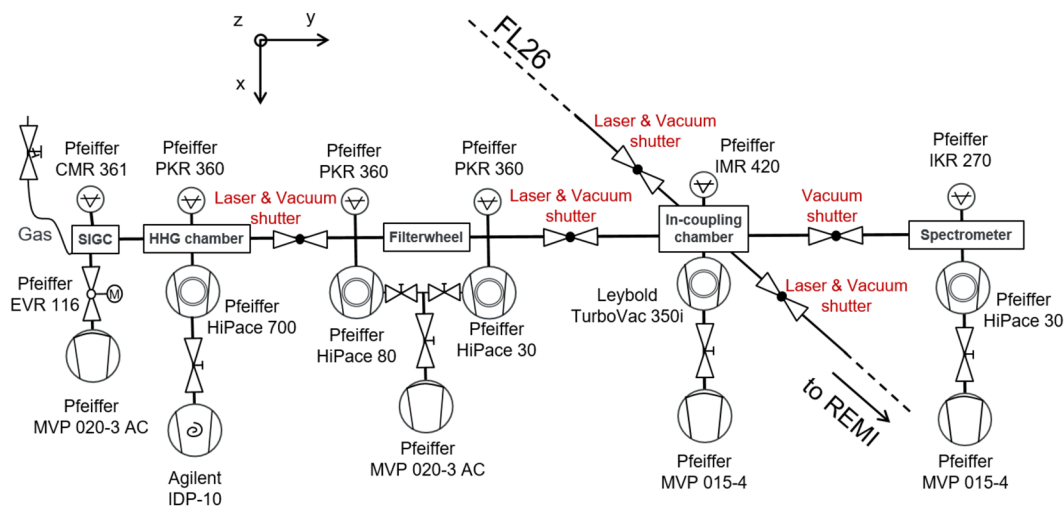


**FIG. 10.** Overview of the complete vacuum system of the VUV beamline. All the vacuum components (pressure gauges, pumps, and valves) and the laser and/or vacuum shutters connected to each section are noted.



were pressed, etc.), the first shutter will close automatically. In the near future, two additional shutters of FL26, placed upstream and downstream of the in-coupling chamber (Fig. 10), will be also integrated into the laser interlock system in order to ensure the protection of the FEL beamline from stray radiation in the case of violation of the interlock conditions.

The vacuum interlock system is currently under development. It is an extension of the already existing vacuum control of the FL26 beamline, developed to control remotely all the vacuum parts, including shutters, and to protect the ultra-high vacuum of the REMI endstation ( $\sim 10^{-11}$  mbar) and the vacuum conditions in the beamline upstream toward the FLASH tunnel. The threshold pressure at the intersection point of the VUV and FL26 beamlines, i.e., the in-coupling chamber, is set at  $1 \times 10^{-7}$  mbar. When this limit is exceeded, the interlock system is triggered and the shutters upstream and downstream of the in-coupling chamber in the FEL beamline close and are not allowed to open again before the pressure recovers. All the vacuum parts of the VUV beamline (see Fig. 10) are currently being integrated into the vacuum control system, and more thresholds will be set for the individual sections.

The three non-transparent shutters (Laser & Vacuum shutters in Fig. 10) of the four around the in-coupling chamber have to be monitored and controlled by both the laser and the vacuum interlock system. For this reason, shutters with two position indicators are used and a complex interlock concept is being implemented in order to control them.

### III. EXPERIMENTAL CONDITIONS

#### A. Differential pumping system

The connection of a high-pressure gas target (necessary for the HHG process) to an ultra-high vacuum FEL beamline was one of the main challenges to address in the beamline construction. Therefore, since the first stages of the technical design of the beamline, it has been important to take into consideration the expected pressure in the different sections of the experimental apparatus. While typically the pressure of the gas medium required for HHG is in a range from a few to hundreds of mbar, the requirement for ultra-high vacuum conditions in REMI under operation limits the pressure to  $10^{-11}$  mbar in this section. In addition to the differential pumping stages already existing in the FL26 beamline (more details in the work of Schmid *et al.*<sup>34</sup>), more stages were installed in the VUV beamline in order to achieve a decrease in pressure by more than 11 orders of magnitude from the SIGC to REMI. The crucial position for the VUV setup is the intersection point with the FEL beamline, where the pressure has to be kept below  $1 \times 10^{-7}$  mbar.

The design of the vacuum beamline is based on the concept of pumping down the greatest part of the gas load from the SIGC in the first section inside the HHG chamber. Provided that the pressure after this position is kept  $\ll 1 \times 10^{-2}$  mbar, the molecular flow description applies. In this regime, the maximum gas flow through the beamline is defined by the geometrical dimensions of the pipes connecting the different vacuum sections. Following this simple concept, one can estimate the vacuum beamline performance and optimize the design with the most convenient choice of differential pumping stages and pumping speeds.

As previously mentioned, the laser-drilled hole in the termination plate of the SIGC acts as a first differential pumping stage. The

mass flow rate  $\dot{m}$  (expressed in g/s) through the opening in the plate can be simulated following the free jet expansion description from the work of Miller,<sup>41</sup>

$$\dot{m} = P_0 A^* \left[ \frac{\gamma W}{RT_0} \left( \frac{2}{\gamma + 1} \right)^{(\gamma+1)/(\gamma-1)} \right]^{1/2}, \quad (2)$$

where  $P_0$  is the “reservoir” pressure in the SIGC,  $A^*$  is the opening area in the plate,  $\gamma = 5/3$  is the adiabatic index for noble gases,  $W$  is the gas molar mass,  $R$  is the ideal gas constant, and  $T_0$  is the reservoir temperature. The average pressure after the plate depends on the gas flow rate  $q_1 = \dot{m}RT_0/W$  (expressed in mbar l/s) divided by the effective pumping speed of the turbo pump used. This estimation allows us to choose a turbo pump speed sufficiently high in order to eliminate most of the gas in this first stage. For instance, considering argon as a generation medium and a maximum reservoir pressure of 500 mbar, the estimated gas flow rate equals  $q_1 = 0.7$  mbarl/s for a  $100 \mu\text{m}$  hole on the SIGC termination plate. In our design, a turbo pump HiPace700 (Pfeiffer Vacuum GmbH) was then installed directly after the gas cell (see Fig. 10). The pump provides a maximum argon pumping speed of 670 l/s, which allows for a HHG chamber average pressure in the  $1 \times 10^{-3}$  mbar range, ensuring the molecular flow regime even for such high reservoir pressure.

A second differential pumping stage is placed between the HHG chamber and the rest of the beamline. It consists of a 5 cm long steel tube welded on a double-sided blind flange (see the inset of Fig. 11) with 4 mm inner diameter. In the molecular flow regime, the length  $l$  and the inner diameter  $d$  of the tube determine the vacuum conductance  $C$  (expressed in l/s),

$$C = \pi \bar{v} \frac{d^3}{12 l}, \quad (3)$$

where  $\bar{v}$  is the mean thermal velocity of the gas. In the specific case of argon as a generating medium, the estimated conductance of the differential pumping tube is then  $C = 0.13$  l/s. Once more, the final average pressure after the differential pumping stage can be calculated from the gas flow rate  $q_2 = C \cdot \Delta P$  and the effective pumping speed of the used turbo pump. In this case, for an argon reservoir pressure of 500 mbar, an effective pumping speed of about 29 l/s allows for a final pressure close to  $5 \times 10^{-6}$  mbar. In our design, a turbo pump HiPace80 (Pfeiffer Vacuum GmbH) was chosen, which ensures a sufficient high pumping speed.

The same calculation can be done for the two remaining differential pumping stages. The filterwheel itself can be considered as a third stage: the difference in diameter between the filterwheel flanges and the beamline leads to a change in the pipe conductance. Gas molecules are therefore trapped in the larger volume of the filterwheel and do not reach the beamline sections downstream. Since most of the gas load is already eliminated in the first two pumping stages, a smaller turbo pump (HiPace30, Pfeiffer Vacuum GmbH) was chosen in this case. The fourth differential pumping stage consists of an additional small tube installed on the input of the in-coupling chamber. For this position, we chose an inner diameter of 10 mm and a tube length of 8 cm to ensure that the full divergent VUV beam can pass through the pipe. Due to the considerable volume of the in-coupling chamber, in the calculation of the final pressure at this position we included a correction for the



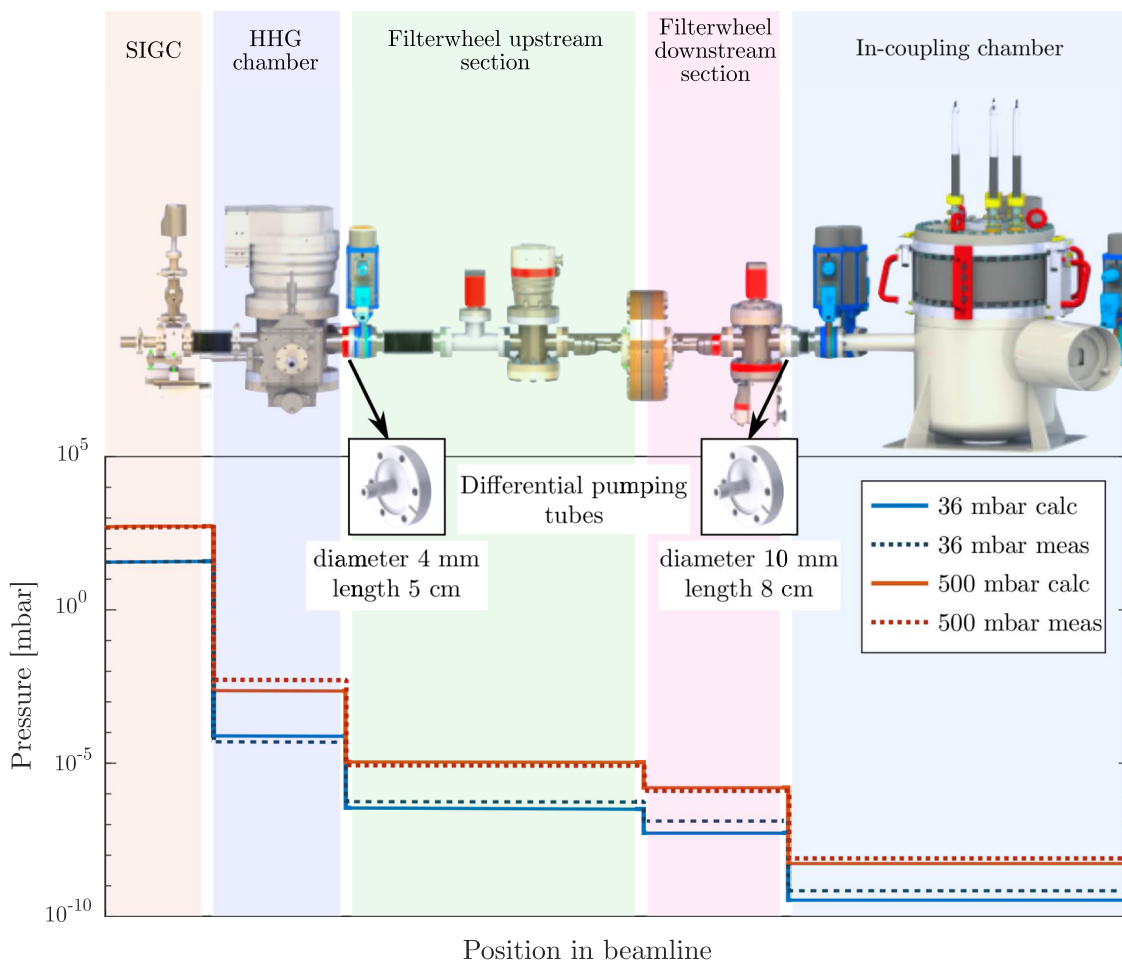


**FIG. 11.** Overview of the pressure in the VUV setup up to the crossing point with the FEL beamline. The calculated (continuous lines) and measured values (dashed lines) for two different reservoir argon pressures in the SIGC.

outgassing from the inner surface of the chamber ( $1.2 \times 10^{-12}$  mbar  $l s^{-1} cm^{-2}$  from Ref. 42, baked for 2 days at 120 °C). An additional tube of 20 mm inner diameter and 5 cm total length is placed at the entrance of the in-line spectrometer assembly to further isolate the in-coupling chamber from the spectrometer, for which the vacuum requirements are less strict.

Following this description, the expected pressure for all the beamline sections between the HHG source and the in-coupling chamber can be estimated. The result is depicted in Fig. 11 (continuous lines) for 36 and 500 mbar of argon in the SIGC. The dashed lines indicate the respective measured pressures. The calculated and measured values are in good agreement with only minor differences. For both reservoir pressure levels considered, an operation pressure  $< 1 \times 10^{-7}$  mbar can be ensured in the in-coupling chamber. A more rigorous pressure estimation should take into account the outgassing contribution along the beamline and the geometrical shape of each component, especially of the filterwheel, which presents a complex inner structure. Nevertheless, the simple model presented here provided a useful tool during the beamline design phase.

## B. VUV pulse energy measurements

In the absence of an energy calibrated spectrometer able to record the full spectrum, the correct analysis of the data from the photodiode detector is of fundamental importance for absolute estimations of the VUV pulse energy. In the setup currently in use, the signal from the photodiode is amplified by using a low-noise current-to-voltage preamplifier (SR570, Stanford Research Systems) and read out by using an oscilloscope (DPO 5204, Tektronix) outside the vacuum system. The charge  $Q_{\text{pulse}}$  produced by the detector per pulse is proportional to the integral of the recorded trace  $S(t)$  over the burst time (expressed in V s), after the removal of any possible offset,

$$Q_{\text{pulse}} = \frac{1}{n_p} \cdot G \cdot \int_{t_0}^{t_1} S(t) dt, \quad (4)$$

where  $n_p$  is the number of pulses in one trace and  $G$  is the effective preamplifier gain or sensitivity in A/V.

From Eq. (4), one can estimate the VUV pulse energy at the source position taking into consideration the photodiode responsivity (A/W) indicated in the detector datasheet and the presence of filters. All filters in the filterwheel and in front of the photodiode block not only the remaining fundamental radiation but part of the generated VUV light as well. In general, the photodiode responsivity  $R(\lambda)$  and the filters transmission  $T(\lambda)$  are functions of the wavelength of the detected radiation. For this reason, the full spectrum of the generated VUV beam would have to be directly recorded and resolved using the spectrometer without the presence of any filter. If the harmonic peaks are narrow enough, they can be assigned to discrete wavelengths  $\lambda$ . By knowing the relative weight  $\eta(\lambda) \leq 1$  for each harmonic order, the energy per pulse of the full spectrum can be written as

$$E_{\text{pulse}} = k \cdot \sum_{\lambda} \eta(\lambda), \quad (5)$$

where  $k$  is an unknown scale factor expressed in J. The charge generated by the photodiode can thus be expressed in the following form:

$$Q_{\text{pulse}} = k \cdot \sum_{\lambda} (\eta(\lambda) \cdot T(\lambda) \cdot R(\lambda)). \quad (6)$$

By combining Eqs. (5) and (6), the pulse energy can be calculated from the following equation:

$$E_{\text{pulse}} = \frac{Q_{\text{pulse}} \cdot \sum_{\lambda} \eta(\lambda)}{\sum_{\lambda} (\eta(\lambda) \cdot T(\lambda) \cdot R(\lambda))} \quad (7)$$

if all the quantities are known or directly measured.

However, the in-line spectrometer installed at the beamline cannot record the full VUV spectrum at once with sufficient resolution and reliability. The third and fifth orders have to be excluded due to stray light, so  $\eta(\lambda)$  is not known for all  $\lambda$ . On the other hand, the photodiode detects radiation only in the range from 30 to 65 nm since the presence of Al filters limits the minimum photon energy transmitted. In this energy range, both  $T(\lambda)$  and  $R(\lambda)$  can be assumed to be constant since only minor fluctuations around a

mean value occur. Equation (7) is then simplified to

$$E_{\text{pulse}} = \frac{Q_{\text{pulse}}}{T \cdot R} = \frac{1}{n_p} \cdot \frac{G}{T \cdot R} \cdot \int_{t_0}^{t_1} S(t) dt. \quad (8)$$

During commissioning of the VUV beamline, a total number of 80 pulses per burst was used with an effective preamplifier sensitivity of  $G = 1 \times 10^{-6}$  A/V. Two 0.1  $\mu\text{m}$  thick aluminum filters (Ni-mesh supported) were present in the VUV beam path up to the photodiode, leading to a total transmission  $T$  of 46%, omitting possible oxidation of the foil used. The photodiode responsivity equals 0.26 A/W in the wavelength range of interest. A small contribution of the 11th harmonic at 71 nm was neglected since the corresponding filter transmission and photodiode responsivity are lower (36% and 0.22 A/W, respectively; see also Fig. 13, Sec. IV).

From the total pulse energy, one can calculate the VUV photon flux taking into account the relative heights  $\eta(\lambda)$  of the harmonic peaks in the spectrum. It should be noted that, since the harmonic orders  $\leq 11$  are not included in the photodiode signal, the pulse energy calculated should be considered as a lower bound of the actually generated signal. In addition, the transmission of aluminum filters strongly depends on the oxidation degree of the foil, which occurs even after brief exposure to air. For a correct pulse energy estimation, the filter transmission should then be directly measured.

The presented analysis relies on the values of the photodiode responsivity provided by the detector datasheet. In order to confirm the validity of our approach, a second identical photodiode AXUV576 was tested using a known infrared source. Figure 12(a) shows a scheme of the experimental setup employed. The output of a Light Conversion PHAROS laser system (1025 nm central wavelength, 8.4 nm spectral bandwidth, and 212 fs pulse duration) was set to 300 mW at 10 kHz repetition rate by an internal pulse picking option. The beam was further attenuated by a half-wave plate combined with a thin-film polarizer in the range of 1–10 mW. A neutral density (ND) filter (ND50A-B, Thorlabs, Inc.) was placed in front of the detector. By measuring the power of the laser beam and taking into account the transmission of the ND filter, the pulse energy that reached the photodiode was estimated. The signal from the detector

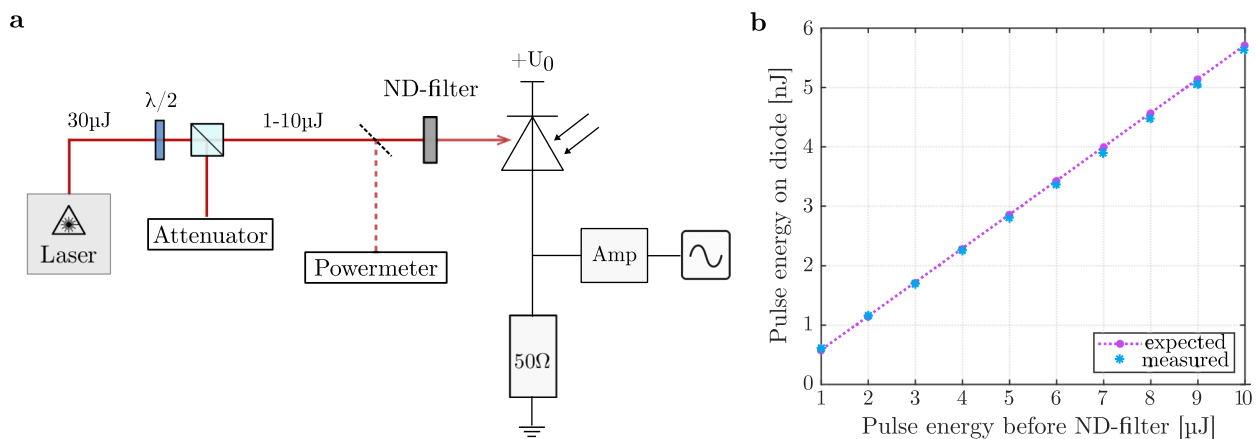


**FIG. 12.** Photodiode pulse energy measurement test. (a) Scheme of the experimental setup for the photodiode test with a secondary laser source. (b) Comparison between the measured and expected IR pulse energies.

was then amplified by using the same preamplifier used in the VUV beamline and analyzed using Eq. (8). The pulse energy measured and the one estimated by the photodiode analysis are in excellent agreement for the full investigated range, as shown in Fig. 12(b).

### C. In-coupling and alignment into FL26

The alignment of the in-coupling mirror was one of the most important and challenging parts of the beamline development. First, the in-coupling chamber had to be installed in the right position and with the right orientation with respect to the FL26 beamline. Translation stages on the granite post, where the chamber lies, in combination with bellow connections between the chamber and both beamlines, provide flexibility in all directions. The chamber was aligned according to the design with respect to references already existing in the experimental hall and on FL26.

The next step was the transfer of information about the position of the inner components of the chamber to the outside by setting additional references (fiducialization), assuming that the delivery position of the hexapod was the nominal position according to the design. This procedure was carried out outside of the chamber with the help of a dummy mirror. Thus, references were placed on the top flange. After replacing the dummy mirror with the real one, the whole structure was mounted on the chamber. Based on the references on the top flange, the whole chamber was aligned in a way that the mirror inside would be (roughly) aligned with respect to the FEL beamline.

The fine alignment had to be done with the VUV beam incident on the mirror and by moving the hexapod mechanism. Due to its low intensity, the VUV beam is visible only on the interaction screen placed in the focus position inside REMI. However, guiding the VUV beam through the FL26 beamline to this position, with several differential pumping tubes and apertures in the way,<sup>34</sup> was too challenging as a first attempt. For this reason, the fundamental NIR beam was observed instead and aligned first on Ce:YAG screens in front of the split-and-delay unit and behind REMI. By using movable apertures as a reference, the NIR beam was aligned 7.5 mm higher than the FEL by tilting the mirror in steps. At every step, the beam position on the mirror was monitored with the chamber camera and corrected by translating the mirror parallel to its surface. After this procedure, the VUV beam was finally observed and spatially overlapped with the FEL beamline alignment laser on the REMI interaction screen. Reference marks were also set on the camera images of all the screens, ensuring well-defined positions for the future VUV beam alignment procedures. The final adjustment of the spatial overlap with the FEL beam on the focus needs to be done during the preparation time of every experiment that makes use of the HHG source.

## IV. PRELIMINARY RESULTS AND DISCUSSION

Preliminary results on the performance of the VUV source are presented in detail by Appi *et al.*<sup>32</sup> The generation of VUV radiation in the range 10–45 eV was achieved. The spectrum was resolved using a 1850 lines/mm grating with a grating–detector distance of 8 cm. Harmonics of the driven wavelength, starting from the seventh order, were resolved on the phosphor screen and captured by using the camera. By integrating the signal along the  $z$  axis, a one-dimensional representation of the spectrum was obtained, as shown

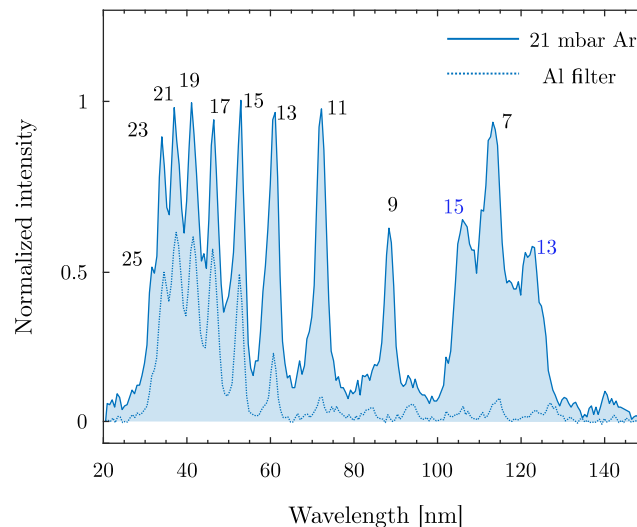


**FIG. 13.** VUV spectrum obtained with 21 mbar of argon in the SIGC. The dashed line represents the spectrum recorded after insertion of a  $0.1 \mu\text{m}$  Al filter in the beam path. The numbers indicate the harmonic orders.

in Fig. 13. In the data reported, the filtered spectrum is plotted with the dotted line and is in perfect agreement with the wavelength calibration. A minimum VUV wavelength of 31 nm, corresponding to the 25th harmonic order, was observed with a pressure of 21 mbar of argon in the SIGC. Secondary peaks around the seventh order correspond to the grating's second order of diffraction, which is not completely suppressed.

The signal was also recorded with the photodiode. The analysis described in Sec. III B for the estimation of the VUV pulse energy can be performed during the experiments for optimization of the generation conditions. An example is shown in Fig. 14, where the trend of the VUV pulse energy is presented as a function of the

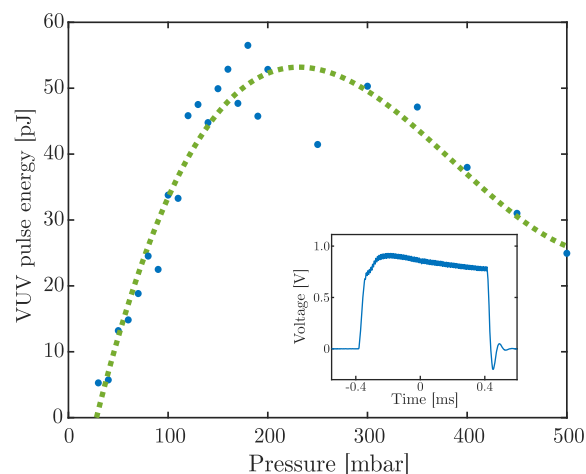


**FIG. 14.** Trend of the VUV pulse energy with respect to the pressure in the SIGC. The pulse energy is estimated from the photodiode trace (inset) and corrected for the beamline losses.

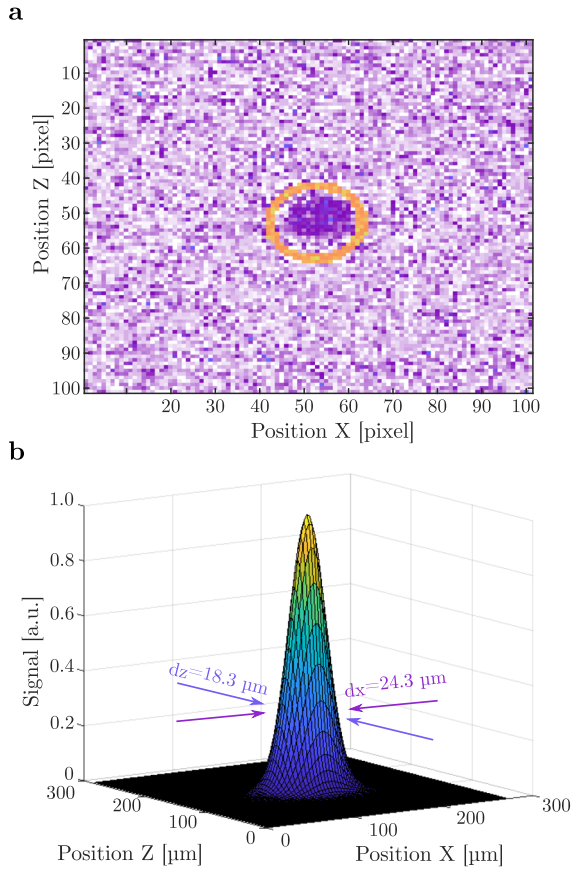


**FIG. 15.** (a) VUV beam visible on the interaction region screen in REMI. The orange curve represents the target position for the FEL beam. (b) 2D-Gaussian fit of the VUV spot in REMI. A  $(1/e^2)$  beam diameter of  $24.3(5) \mu\text{m}$  and  $18.3(4) \mu\text{m}$  is estimated for the x and z axis, respectively.

gas pressure in the SIGC. The signal reaches a maximum at about 200 mbar and then decreases. In order to minimize the effect of shot-to-shot energy variations, every trace (see the inset of Fig. 14) is an average of 600 pulse trains (bursts). The total VUV pulse energy depends on the conversion efficiency of the HHG process and on the fundamental laser pulse energy. Thus, the generation conditions, including the focusing system of the driving laser, have to be optimized according to the laser performance during the experiment. In the preliminary tests carried out at the VUV beamline, a harmonic pulse energy of 0.1 nJ in the 20–40 eV range was estimated (number of photons per pulse in the order of  $10^7$  and conversion efficiency in the order of  $10^{-7}$ ).<sup>32</sup>

By inserting the hyperboloidal mirror in the beam path, the VUV radiation is sent toward the REMI endstation. For fine adjustments of the mirror alignment, the VUV beam position can be monitored on the interaction screen [see Fig. 15(a)]. By a 2D-Gaussian fit of the image, the size of the beam on the screen is estimated by taking into account the size of the camera pixel ( $3.75 \times 3.75 \mu\text{m}^2$ ) and the magnification factor ( $\sim 2.4$ ) of the camera system. Thus, one pixel corresponds to  $\sim 1.56 \mu\text{m}$  on the screen. For a focusing system of the NIR pulses with focal lengths of 500 mm and  $-300$  mm for F3 and F4, respectively, at a 165 mm distance (see Fig. 2), the size of the observed focused beam ( $1/e^2$  diameter) in REMI was estimated at  $24.3(5) \mu\text{m}$  in the x axis and  $18.3(4) \mu\text{m}$  in the z axis [Fig. 15(b)]. A comparison with the simulated focus size (depicted in Fig. 9) indicates a VUV source size of  $<50 \mu\text{m}$ . The movement of the focused beam on the REMI screen by less than 2 pixels upon re-insertion of the mirror in the beam path indicates the good repeatability of the mirror's position. Such a small beam misalignment can be easily corrected with the hexapod mechanism.

During commissioning of the VUV beamline, the focused VUV beam in REMI was used in a first proof-of-principle experiment<sup>32</sup> on argon photoionization. Since the first ionization potential  $I_p$  of argon is 15.8 eV,<sup>43</sup> photoionization events are expected by all the harmonic orders  $\geq 11$  (17.5 eV). The reaction microscope allows us

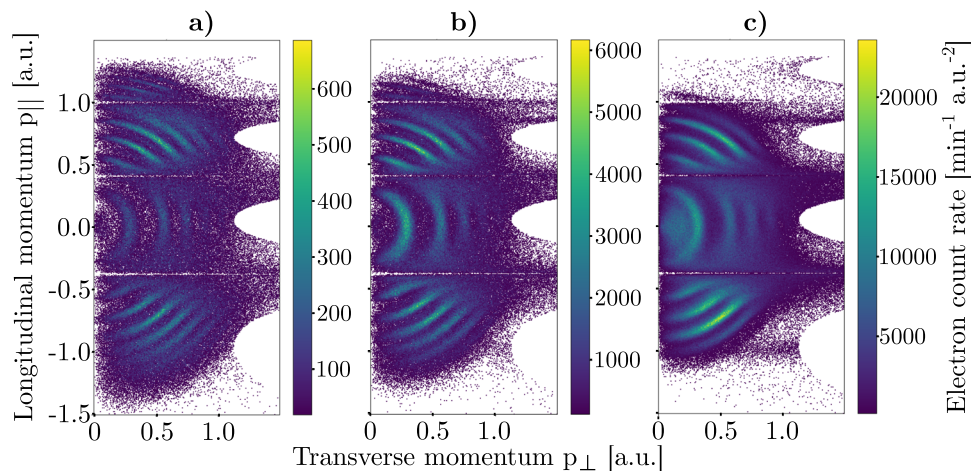


**FIG. 16.** Argon photoelectron momentum distributions in the transverse and longitudinal direction with respect to the VUV polarization axis. Half circles correspond to electrons of constant kinetic energy. The brightness indicates the electron count rate. VUV radiation was generated in 40 mbar of argon (a), 40 mbar of krypton (b), and 35 mbar of xenon (c), respectively. Instead of a filter, a 4 mm aperture was used to block most of the divergent fundamental beam.



to detect ions and electrons from these photoionization events and to reconstruct the photoelectron momenta. An example is depicted in Fig. 16 for three different gases used as generation media in the HHG source. The 2D-distributions are shown as functions of the longitudinal and transverse momentum,  $p_{\parallel}$  and  $p_{\perp}$ , with respect to the VUV beam polarization axis, in cylindrical coordinates. As expected, several discrete lines of constant kinetic energy are present, each one corresponding to a specific photon energy of the VUV harmonic spectrum. The event rate of singly ionized argon measured in the reaction microscope provided an estimation of the VUV source stability over time. Fluctuations of the ion rate of less than 20% during a 14-h-long measurement indicated a sufficiently stable operation for future pump–probe experiments. The complete results and discussion of this first VUV photoionization experiment are presented by Appi *et al.*<sup>32</sup>

## V. OUTLOOK

In this work, we described the technology and the experimental parameters that were employed for the first setup combining a HHG-based source with high-flux FEL pulses in a REMI endstation.<sup>32,35</sup> In light of the results achieved, the new setup offers a wide range of opportunities for ultrafast time-resolved spectroscopy of atoms and molecules. In particular, prototypical FEL-HHG pump–probe experiments can be envisioned, in which broadband valence and site-selective core excitations are simultaneously achieved. In addition, the same scheme is ideal to trigger charge dynamics initiating a chemical reaction and selectively probe it via core-level photo-ionization. Furthermore, the high peak intensity of FEL pulses allows such processes to be interrogated in atoms and molecules while triggering specific nonlinearities. This approach would be crucial to investigate, and possibly control, charge dynamics beyond the linear regime upon soft x-ray irradiation. So far, the above-mentioned studies have been extremely challenging or even out of reach, while promising to have a large impact in a variety of fields, from chemistry to photo-biology.<sup>44,45</sup> The challenges mostly originate from the constraints of FEL-only or HHG-only experiments in terms of temporal resolution and fluence, respectively. The HHG-FEL setup presented here is promising to overcome such limitations and represents a cutting-edge experimental tool for a new family of time-resolved spectroscopical studies.

Recently, an XUV spectrometer was also installed behind the reaction microscope in the FL26 beamline at FLASH2, paving the way for transient absorption spectroscopy experiments on atomic and molecular targets in the gas phase.<sup>46,47</sup> In addition to time-resolved spectroscopy of atoms and molecules, the interaction between FEL and HHG photons offers a unique opportunity for the implementation of all-optical holographic methods to characterize FEL waveforms on a single-shot basis. Such a scheme was recently employed in a table-top setup for the full characterization of attosecond pulses<sup>48</sup> and may represent a very useful diagnostic tool to be implemented at FEL facilities. We also foresee that the HHG source installed in the vicinity of a FEL beamline could be potentially used by FEL users to perform preliminary experiments to optimize sample preparation, detection and, more generally, their experimental setup prior to FEL beamtimes.

## ACKNOWLEDGMENTS

We acknowledge funding from the Bundesministerium für Bildung und Forschung (BMBF) through the project “Synchrone VUV-Lichtquelle am FLASH II”; from the clusters of excellence “Quantum Frontiers” (EXC-2123-A05) and “PhoenixD” (EXC-2122); and from DESY, LUH, and MPIK. The publication of this article was funded by the Leibniz Universität Hannover.

## AUTHOR DECLARATIONS

### Conflict of Interest

The authors have no conflicts to disclose.

### Author Contributions

E.A., C.C.P., J.L.M., T.L., S.A., C.M.H., B.M., and M.K. designed the VUV beamline. J.S. performed ray tracing simulations for the in-coupling mirror. T.F. and optiX fab GmbH designed and manufactured the in-coupling mirror. E.A., C.C.P., M. Braune, and M. Brachmanski constructed the VUV beamline. E.A., C.C.P., and S.A. developed and maintained the optical setup. E.A., C.C.P., C.J., and P.M. conducted the experiments on VUV generation. E.A. and C.C.P. analyzed the VUV spectrometer and photodiode data. C.M.H. and A.S. performed the test experiment with the second photodiode. E.A., C.C.P., H.L., and F.T. conducted the experiments at the REMI endstation. P.S., S.M., and H.L. analyzed the REMI data. A.T. and F.C. contributed to the introduction and outlook. R.T., I.H., R.M., U.M., and M.K. devised the experiments. All the authors participated in the realization of the manuscript.

## DATA AVAILABILITY

The data that support the findings of this study are available from the corresponding author upon reasonable request.

## REFERENCES

- 1 C. Feng and H.-X. Deng, *Nucl. Sci. Tech.* **29**, 160 (2018).
- 2 R. Schoenlein, T. Elsaesser, K. Hollnack, Z. Huang, H. Kapteyn, M. Murnane, and M. Woerner, *Philos. Trans. R. Soc., A* **377**, 20180384 (2019).
- 3 E. A. Seddon, J. A. Clarke, D. J. Dunning, C. Masciovecchio, C. J. Milne, F. Parmigiani, D. Rugg, J. C. H. Spence, N. R. Thompson, K. Ueda *et al.*, *Rep. Prog. Phys.* **80**, 115901 (2017).
- 4 M. Khalil and S. Mukamel, *J. Chem. Phys.* **153**, 100401 (2020).
- 5 A. Nilsson, J. LaRue, H. Öberg, H. Ogasawara, M. Dell’Angela, M. Beye, H. Öström, J. Gladh, J. K. Nørskov, W. Wurth *et al.*, *Chem. Phys. Lett.* **675**, 145 (2017).
- 6 R. Moshhammer and K. Schnorr, *Synchrotron Light Sources and Free-Electron Lasers: Accelerator Physics, Instrumentation and Science Applications* (Springer, Cham, Denmark, 2020), p. 1493.
- 7 T. Pfeifer, C. Spielmann, and G. Gerber, *Rep. Prog. Phys.* **69**, 443 (2006).
- 8 J. Ullrich, A. Rudenko, and R. Moshhammer, *Annu. Rev. Phys. Chem.* **63**, 635 (2012).
- 9 P. M. Kraus, M. Zürch, S. K. Cushing, D. M. Neumark, and S. R. Leone, *Nat. Rev. Chem.* **2**, 82 (2018).
- 10 J. M. Martin-Garcia, C. E. Conrad, J. Coe, S. Roy-Chowdhury, and P. Fromme, *Arch. Biochem. Biophys.* **602**, 32 (2016).
- 11 J. Miao, T. Ishikawa, I. K. Robinson, and M. M. Murnane, *Science* **348**, 530 (2015).
- 12 R. Neutze and K. Moffat, *Curr. Opin. Struct. Biol.* **22**, 651 (2012).



- <sup>13</sup>G. Kastirke, M. S. Schöffler, M. Weller, J. Rist, R. Boll, N. Anders, T. M. Baumann, S. Eckart, B. Erk, A. De Fanis *et al.*, *Phys. Rev. X* **10**, 021052 (2020).
- <sup>14</sup>J. Duris, S. Li, T. Driver, E. G. Champenois, J. P. MacArthur, A. A. Lutman, Z. Zhang, P. Rosenberger, J. W. Aldrich, R. Coffee *et al.*, *Nat. Photonics* **14**, 30 (2020).
- <sup>15</sup>E. Lindroth, F. Calegari, L. Young, M. Harmand, N. Dudovich, N. Berrah, and O. Smirnova, *Nat. Rev. Phys.* **1**, 107 (2019).
- <sup>16</sup>C. M. Heyl, C. L. Arnold, A. Couairon, and A. L'Huillier, *J. Phys. B: At., Mol. Opt. Phys.* **50**, 013001 (2016).
- <sup>17</sup>F. Calegari, G. Sansone, S. Stagira, C. Vozzi, and M. Nisoli, *J. Phys. B: At., Mol. Opt. Phys.* **49**, 062001 (2016).
- <sup>18</sup>M. Reduzzi, P. Carpeggiani, S. Kühn, F. Calegari, M. Nisoli, S. Stagira, C. Vozzi, P. Dombi, S. Kahaly, P. Tzallas *et al.*, *J. Electron Spectrosc. Relat. Phenom.* **204**, 257 (2015).
- <sup>19</sup>S. Kühn, M. Dumergue, S. Kahaly, S. Mondal, M. Füle, T. Csizmadia, B. Farkas, B. Major, Z. Várallyay, E. Cormier *et al.*, *J. Phys. B: At., Mol. Opt. Phys.* **50**, 132002 (2017).
- <sup>20</sup>L. Gallmann, C. Cirelli, and U. Keller, *Annu. Rev. Phys. Chem.* **63**, 447 (2012).
- <sup>21</sup>F. Krausz and M. Ivanov, *Rev. Mod. Phys.* **81**, 163 (2009).
- <sup>22</sup>M. Nisoli, P. Decleva, F. Calegari, A. Palacios, and F. Martín, *Chem. Rev.* **117**, 10760 (2017).
- <sup>23</sup>A. S. Johnson, T. Avni, E. W. Larsen, D. R. Austin, and J. P. Marangos, *Philos. Trans. R. Soc., A* **377**, 20170468 (2019).
- <sup>24</sup>J. Li, J. Lu, A. Chew, S. Han, J. Li, Y. Wu, H. Wang, S. Ghimire, and Z. Chang, *Nat. Commun.* **11**, 2748 (2020).
- <sup>25</sup>P. B. Corkum, *Phys. Rev. Lett.* **71**, 1994 (1993).
- <sup>26</sup>M. Lewenstein, P. Balcou, M. Y. Ivanov, A. L'Huillier, and P. B. Corkum, *Phys. Rev. A* **49**, 2117 (1994).
- <sup>27</sup>X. Ren, J. Li, Y. Yin, K. Zhao, A. Chew, Y. Wang, S. Hu, Y. Cheng, E. Cunningham, Y. Wu, M. Chini, and Z. Chang, *J. Opt.* **20**, 023001 (2018).
- <sup>28</sup>L. Young, K. Ueda, M. Gühr, P. H. Bucksbaum, M. Simon, S. Mukamel, N. Rohringer, K. C. Prince, C. Masciovecchio, M. Meyer *et al.*, *J. Phys. B: At., Mol. Opt. Phys.* **51**, 032003 (2018).
- <sup>29</sup>I. Pupeza, C. Zhang, M. Högner, and J. Ye, *Nat. Photonics* **15**, 175 (2021).
- <sup>30</sup>W. Ackermann, G. Asova, V. Ayvazyan, A. Azima, N. Baboi, J. Bähr, V. Balandin, B. Beutner, A. Brandt, A. Bolzmann *et al.*, *Nat. Photonics* **1**, 336 (2007).
- <sup>31</sup>B. Faatz, E. Plönjes *et al.*, *New J. Phys.* **18**, 062002 (2016).
- <sup>32</sup>E. Appi, C. C. Papadopolou, J. L. Mapa, N. Wesavkar, C. Jusko, P. Mosel, S. Ališauskas, T. Lang, C. M. Heyl, B. Manschwetus *et al.*, *Sci. Rep.* **10**, 6867 (2020).
- <sup>33</sup>R. Moshhammer, M. Unverzagt, W. Schmitt, J. Ullrich, and H. Schmidt-Böcking, *Nucl. Instrum. Methods Phys. Res., Sect. B* **108**, 425 (1996).
- <sup>34</sup>G. Schmid, K. Schnorr, S. Augustin, S. Meister, H. Lindenblatt, F. Trost, Y. Liu, M. Braune, R. Treusch, C. D. Schröter, T. Pfeifer, and R. Moshhammer, *J. Synchrotron Radiat.* **26**, 854 (2019).
- <sup>35</sup>S. Meister, H. Lindenblatt, F. Trost, K. Schnorr, S. Augustin, M. Braune, R. Treusch, T. Pfeifer, and R. Moshhammer, *Appl. Sci.* **10**, 2953 (2020).
- <sup>36</sup>T. Lang, S. Alisaukas, U. Große-Wortmann, T. Hülsenbusch, B. Manschwetus, C. Mohr, J. Müller, F. Peters, N. Schirmel, S. Schulz, A. Swiderski, J. Zheng, and I. Hartl, in *2019 Conference on Lasers and Electro-Optics Europe European Quantum Electronics Conference (CLEO/Europe-EQEC)* (IEEE, 2019), p. 1.
- <sup>37</sup>S. Schulz, I. Grguraš, C. Behrens, H. Bromberger, J. T. Costello, M. K. Czwalinna, M. Felber, M. C. Hoffmann, M. Ilchen, H. Y. Liu *et al.*, *Nat. Commun.* **6**, 5938 (2015).
- <sup>38</sup>B. L. Henke, E. M. Gullikson, and J. C. Davis, *At. Data Nucl. Data Tables* **54**, 181 (1993).
- <sup>39</sup>T. Noll, K. Holldack, G. Reichardt, O. Schwarzkopf, and T. Zeschke, *Precis. Eng.* **33**, 291 (2009).
- <sup>40</sup>S. J. Goh, H. J. M. Bastiaens, B. Vratzov, Q. Huang, F. Bijkerk, and K. J. Boller, *Opt. Express* **23**, 4421 (2015).
- <sup>41</sup>D. R. Miller, "Free jet sources," in *Atomic and Molecular Beam Methods* (Oxford University Press, 1988).
- <sup>42</sup>VACOM Vakuum Komponenten & Messtechnik GmbH, White Paper WP00002 Rev. A, 2016.
- <sup>43</sup>S. G. Lias, NIST Chemistry WebBook, NIST Standard Reference Database Number 69, retrieved April 2021.
- <sup>44</sup>V. Stooß, S. M. Cavaletto, S. Donsa, A. Blättermann, P. Birk, C. H. Keitel, I. Březinová, J. Burgdörfer, C. Ott, and T. Pfeifer, *Phys. Rev. Lett.* **121**, 173005 (2018).
- <sup>45</sup>C. Ott, L. Aufleger, T. Ding, M. Rebholz, A. Magunia, M. Hartmann, V. Stooß, D. Wachs, P. Birk, G. D. Borisova *et al.*, *Phys. Rev. Lett.* **123**, 163201 (2019).
- <sup>46</sup>T. Ding, M. Rebholz, L. Aufleger, M. Hartmann, V. Stooß, A. Magunia, P. Birk, G. D. Borisova, C. da Costa Castanheira, P. Rupprecht *et al.*, *Faraday Discuss.* **228**, 519 (2021).
- <sup>47</sup>M. Rebholz, T. Ding, V. Despré, L. Aufleger, M. Hartmann, K. Meyer, V. Stooß, A. Magunia, D. Wachs, P. Birk *et al.*, *Phys. Rev. X* **11**, 031001 (2021).
- <sup>48</sup>O. Pedatzur, A. Trabattoni, B. Leshem, H. Shalmoni, M. C. Castrovilli, M. Galli, M. Lucchini, E. Månsson, F. Frassetto, L. Poletto *et al.*, *Nat. Photonics* **13**, 91 (2019).